Journal of Materials Chemistry B

PAPER

View Article Online
View Journal | View Issue

Cite this: J. Mater. Chem. B, 2015, 3, 4370

Potential theranostic and multimodal iron oxide nanoparticles decorated with rhenium–bipyridine and –phenanthroline complexes†

Sophie Carron,[a] Maarten Bloemen,[a] Luce Vander Elst,[bc] Sophie Laurent,[bc] Thierry Verbiest[a] and Tatjana N. Parac-Vogt*[a]

Received 12th March 2015,
Accepted 17th April 2015

DOI: 10.1039/c5tb00460h

www.rsc.org/MaterialsB

Two structurally similar nanoparticles were designed for multimodal imaging and possible radiotherapy. The assembly consists of ultrasmall superparamagnetic iron oxide nanoparticles that act as contrast agents for MRI with a luminescent rhenium complex, for optical imaging, attached to the surface. Rhenium has the advantage of being luminescent and carries two radio-isotopes ^{186}Re and ^{188}Re making it possible to act as a contrast agent for SPECT (γ) and to be used for radiotherapy (β). The iron oxide nanoparticles were treated with a silane and further functionalized with picolyl. This picolyl was used to capture rhenium(I)$(CO)_3$-1,10-phenanthroline (ReL_1) or rhenium(I)$(CO)_3$-2,2′-bipyridine (ReL_2) and forms the final product Fe_3O_4-picolyl-rhenium(I)$(CO)_3$-1,10-phenanthroline (IO-ReL_1) or Fe_3O_4-silica-picolyl-rhenium(I)$(CO)_3$-2,2′-bipyridine (IO-ReL_2), respectively. All products were characterized properly (TEM, XRD, NMR, IR and TXRF) and a full investigation of the relaxometric and optical properties was conducted. Although iron oxide nanoparticles suffer from strong Rayleigh scattering, an efficient sensitized luminescence was observed and the orange emission wavelength was found to be 585 nm for IO-ReL_1 and 592 nm for IO-ReL_2 after irradiation at 395 nm. The relaxometric study of these ultrasmall nanoparticles showed very promising results. The r_2 values measured at a magnetic field strength of 60 MHz of the nanoparticles being 92.9 mM^{-1} s^{-1} and 97.5 mM^{-1} s^{-1} for IO-ReL_1 and IO-ReL_2, respectively, were at least 1.5 times larger than Sinerem®.

Introduction

The pursuit of generating new classes of multimodal imaging agents for medical diagnostics has gained much interest, especially since the combination of Optical Imaging (OI) and Magnetic Resonance Imaging (MRI) has proven its potential as a preclinical research tool and has shown success *via* non-invasive experiments on mice.[1–6] The most apparent method for creating such a contrast agent lies in designing a hybrid MRI–OI system. A well-known and frequently used material for MRI are superparamagnetic iron oxide nanoparticles, which exhibit a unique response to external magnetic fields.[7] Commercial and under clinical investigation iron oxide nanoparticles include ferumoxides (endorem/feridex), ferumoxtran-10 (sinerem/combidex), ferumoxsil (lumirem/gastromark), and ferucarbotran (resovist). They owe their properties as T_2 agents for influencing the local magnetic field inhomogeneities.[7–9] Ultrasmall superparamagnetic iron oxide nanoparticles (USPIOs) are generally defined by a crystal size of less than 10 nm and are therefore known for their long circulation time in the bloodstream,[10] which makes them interesting for T_1[10,11] and T_2[12] weighted MRI images[12,13] for diagnosis of lymph nodes and brain tumors. Several reports have described potential multimodal contrast agents consisting of an assembly between iron oxide particles and optical imaging probes. The most proposed OI probes with iron oxide nanoparticles are surface plasmon resonance (gold NPs),[14–17] fluorescent lipids,[18] quantum dots (QDs),[19–21] dendrimers,[22,23] organic dyes,[24–27] conjugated polymers[28] or Ln-complexes.[29] These systems show much promise, but suffer from one or more shortcomings. The large total size is unfavorable as it shortens the residence time in the blood stream, and is mostly observed in systems which form hybrid nanoparticle materials or when several iron oxide particles are coated by one lipid strand.[14,18] Some organic dyes are toxic to the human body, which makes them non-bio-compatible.[24] Photo-bleaching and low chemical stability are some of the major drawbacks with organic dyes functionalized with iron oxide nanoparticles.[24] Although a number of biocompatible nanoparticles

[a] Department of Chemistry, KU Leuven, Celestijnenlaan 200F/200D, 3001 Leuven, Belgium. E-mail: tatjana.vogt@chem.kuleuven.be; Fax: +32 (0)16 327992; Tel: +32 (0)16 327612
[b] Department of General, Organic and Biomedical Chemistry, University of Mons, Place du Parc 23, 7000 Mons, Belgium
[c] Center for Microscopy and Molecular Imaging (CMMI), 6041 Gosselies, Belgium

† Electronic supplementary information (ESI) available. See DOI: 10.1039/c5tb00460h

designed with iron oxides have been reported, only a few are clinically approved, as most of them suffer from the detachment of the coating material resulting in highly unfavourable aggregation.[30]

Multimodal systems can have interesting biomedical applications[31] and in this report a new class of hybrid MRI–OI probes is made by using USPIO nanoparticles and sensitized luminescence with a d-block element, rhenium. With this approach some of the previous drawbacks are tackled, mainly focusing on the overall size and the stability of the system. Bimodal iron oxide nanoparticles are generally too large to be excreted *via* kidneys, they are instead internalized by cells of the reticulo-endothelial system.[25] The toxicity of rhenium is not exploited to the fullest but tests of their halide salts have shown very low toxicity levels similar to NaCl.[32,33] A rhenium polymer coated iron oxide assembly was tested to be negative for cytotoxicity in HeLa cells and did not show any toxicity in mice.[34] Another advantage of using rhenium is that it carries two radioisotopes ^{186}Re and ^{188}Re, which are both γ- and β-emitters. This can be of interest for SPECT (γ) or radiotherapy (β).[34] In order to obtain small-sized nanoparticulates, we chose the approach in which a very thin silica shell was formed around the USPIOs to render them water dispersible and accessible for further surface functionalization. Using siloxanes is a convenient synthetic approach to generate a bio-compatible, inert and permanent shell that is well known for its diverse functionalities.[35] We have recently developed a synthetic procedure to create a thin layer of functionalized siloxanes around magnetite (Fe_3O_4) nanoparticles[36] which forms a suitable scaffold for attaching rhenium complexes. In this paper we demonstrate the usefulness of siloxane coated magnetite for creating a potential bimodal contrast agent for MRI and optical imaging.

Materials and methods

Materials

All reagents and solvents were obtained from Acros Organics (Geel, Belgium), ABCR (Karlsruhe, Germany), BDH prolabo (Leuven, Belgium), Sigma-Aldrich (Bornem, Belgium), Alfa Aesar (Ward Hill, USA) and Chemlab (Zedelgem, Belgium) and were used without further purification.

Instrumentation

^{1}H NMR spectra were recorded using a Bruker Avance 300 MHz. IR spectra were measured using a Bruker Vertex 70 FT-IR spectrometer (Bruker, Ettlingen, Germany) equipped with a Platinum ATR accessory and data were processed using OPUS 6.5 software. Rhenium and iron concentrations were detected using a TXRF Bruker S2 Picofox equipped with a Bruker AXS sample carrier. As an internal standard a Chem-Lab gallium(III) standard solution (1000 μg mL^{-1}, 2–5% HNO_3) was further diluted to 20 ppm and was as such used to determine the correct concentrations. X-ray powder diffraction spectra were obtained for oleate capped iron oxide nanoparticles in reflection (Bragg–Brentano geometry) using a Rigaku Rotaflex diffractometer fitted with a Rigaku RU-200B rotating Cu-anode (k = 1.54 Å) at a power of 4 kW. The diffracted X-rays were collected after Ni-filtering on a scintillation counter. Samples were deposited on a glass microscope slide from solution. The vacuum dried Fe_3O_4-ReL_1 and Fe_3O_4-ReL_2 nanoparticles suitable for powder X-ray diffraction were mounted on a nylon loop attached to a copper pin and placed on an Agilent SuperNova diffractometer at room temperature (293 K) using Mo Kα radiation (l = 0.71073 Å) and the absorption corrections were applied using CrysAlisPro.[37] Transmission electron microscopy measurements were performed on a 80 kV Zeiss EM-900 using 300 mesh Formvar/carbon coated copper grids. Distribution data were calculated using ImageJ. Oleate-coated nanoparticles were dispersed in heptane while all other nanoparticles were dispersed in ethanol and subsequently deposited onto the grid. Photon correlation spectroscopy was performed at room temperature using a BIC multiangle laser light scattering system with 90° scattering angle (Brookhaven Instruments Corporation, Holtsville, USA). Analysis was done using Igor Pro 6.20 software. Absorption spectra were measured using a Varian Cary 5000 spectrophotometer on freshly prepared aqua solutions in quartz Suprasil cells (115F-QS) with an optical path length of 1.0 cm. Emission spectra were recorded using an Edinburgh Instruments FS920 steady-state spectrofluorimeter. This instrument was equipped with a 230 mW diode laser (980 nm, Power Technology) and an extended re-sensitive photomultiplier (185–1010 nm, Hamamatsu R 2658P). All spectra were analyzed using Edinburgh software and corrected for the instrumental functions. Proton Nuclear Magnetic Relaxation Dispersion (NMRD) profiles were measured using a Stelar Spinmaster FFC (fast-field cycling NMR relaxometer Stelar, Mede PV, Italy) over a magnetic field strength range that extended from 0.24 mT to 0.7 T. Measurements were performed on samples (0.6 mL) contained in 10 mm (outside diameter) Pyrex tubes. Additional relaxation rates at 20 and 60 MHz were obtained using a Minispec mq20 and a Minispec mq60 (Bruker, Karlsruhe, Germany). The proton NMRD curves were fitted using data-processing software, including different theoretical models describing the nuclear relaxation phenomena (Minuit, CERN Library).[38–40]

Synthesis

***fac*-Chlorotricarbonyl(X)rhenium(I) (X = 1,10-phenanthroline (ReL_1) or 2,2′-bipyridine (ReL_2)).** The compound was prepared according to the literature procedure.[41] ^{1}H NMR (X = 2,2′-bipyridine) (DMSO, 300 MHz): δ (ppm) 7.77 (td, 2H), 8.36 (td, 2H), 8.78 (dd, 2H), 9.03 (dd, 2H). ^{1}H NMR (X = 1,10-phenanthroline) (DMSO, 300 MHz): δ (ppm) 8.12 (t, 2H), 8.34 (s, 2H), 8.99 (dd, 2H), 9.44 (dd, 2H).

***fac*-(Acetonitrile)tricarbonyl(X)rhenium(I) triflate (X = 1,10-phenanthroline (ReL_1) or 2,2′-bipyridine (ReL_2)).** The compound was prepared according to the literature procedure.[42] ^{1}H NMR (X = 2,2′-bipyridine) (DMSO, 300 MHz): δ (ppm) 7.87 (t, 2H), 8.45 (dd, 2H), 8.82 (d, 2H), 9.10 (d, 2H). ^{1}H NMR (X = 1,10-phenanthroline) (DMSO, 300 MHz): δ (ppm) 8.21 (t, 2H), 8.40 (s, 2H), 9.09 (dd, 2H), 9.52 (dd, 2H).

Fe_3O_4-oleate nanoparticles. An iron(oleate)$_3$-precursor (36 g, 40 mmol) was mixed with oleic acid (6.3 mL, 20 mmol) and 1-octadecene (254 mL). This mixture was thermally decomposed

at 593 K for 30 minutes. After cooling down to room temperature, ethanol was added to the resultant black dispersion to precipitate the nanoparticles, which were purified magnetically. The nanoparticles were stored (100 mg mL^{-1}) in heptane for long-term storage.[36]

Fe_3O_4-COOH nanoparticles. 200 mg of Fe_3O_4-oleate nanoparticles, dispersed in heptane, were added to 100 mL of toluene. To this mixture 5 mL of triethylamine, 100 mL of water and 2 mmol of *N*-[(3-trimethoxysilyl)propyl] ethylenediamine triacetic acid trisodium salt were added.[36] This solution was placed in an ultrasonication bath for 5 hours. Afterwards, the particles were placed on a magnet to precipitate the functionalized particles and washed three times with heptane and acetone. Finally, the functionalized nanoparticles were dispersed in water with a concentration of 10 mg mL^{-1}.

Fe_3O_4-picolyl nanoparticles. 10 mg of Fe_3O_4-COOH nanoparticles were sonicated for 10 min and subsequently 50 mg of 1-ethyl-3-(3-dimethylaminopropyl)carbodiimide (EDC) and 50 mg of *N*-hydroxysuccinimide (NHS) were added to the mixture after sonicating the solution for another 5 min with 65 μL of picolylamine. The resultant mixture was left to sonicate for 30 min at room temperature and purification occurred magnetically and the resultant mixture was washed with Et_2O and water. The particles were kept in a solution of 5 mg mL^{-1} in water.

Fe_3O_4-picolyl-rhenium(I)$(CO)_3$-X nanoparticles (X = 1,10-phenanthroline (IO-ReL_1) or 2,2′-bipyridine (IO-ReL_2)). To 5 mg of *fac*-(acetonitrile)tricarbonyl(X)rhenium(I) triflate (X = 1.10-phenanthroline (ReL_1) or 2,2′-bipyridine (ReL_2)) in 5 mL of acetonitrile a solution of 5 mg Fe_3O_4-picolyl nanoparticles in 1 mL of water was added at a pH of 8. The resultant mixture was stirred overnight under an argon atmosphere at 323 K. The purification occurred magnetically and the nanoparticles were washed with Et_2O and water. The particles were kept in a solution of 5 mg mL^{-1} in water.

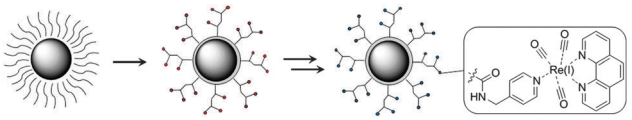

Scheme 1 Design of the magnetoluminescent iron oxide nanoparticles. The oleate capped iron oxide particles were treated with *N*-(trimethoxysilylpropyl)ethylenediamine triacetic acid trisodium salt to obtain hydrophilic iron oxide nanoparticles with multiple acid functions (red circles), followed by multistep synthesis with picolylamine, which reacted with the free acid of the nanoparticles forming a peptide bond and subsequently with rhenium(I) $(CO)_3L_1$.OTf or rhenium(I) $(CO)_3L_2$.OTf to obtain the objective molecule. A magnification of the luminophore (blue circle) is depicted in the square of this scheme. (1,10-Phenanthroline rhenium complex (REL_1) is represented here but also 2,2′-bipyridine rhenium complex (ReL_2) was used in this report).

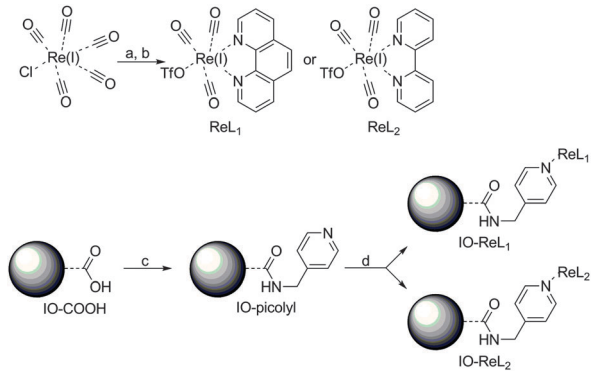

Scheme 2 Synthetic procedure for the IO-ReL_1 and IO-ReL_2 molecules. (a) 2 eq. 1,10-Phenanthroline (L_1) or 2,2′-bipyridine (L_2), 1 eq. $ClRe(CO)_5$, benzene, 333 K, 5 h. (b) AgOTf, THF/MeCN, 16 h. (c) H_2O/THF, HCl, 1-ethyl-3-(3-dimethylaminopropyl)carbodiimide (EDC), *N*-hydroxysuccinimide (NHS), sonicate 30 min. (d) H_2O/CAN, $NaHCO_3$, 223 K, 17 h.

Results and discussion

Design and synthesis

The strategy used to synthesize small monodisperse multimodal iron oxide (IO) nanoparticles with a new type of luminophore attached to the surface is depicted in Scheme 1. In the first step, the oleate capped Fe_3O_4-NPs were treated with acid functionalized siloxanes to yield water dispersible Fe_3O_4-NPs. These acid functions were then reacted with a pyridine derivative to act as an anchor for the luminophore. Rhenium(I) in combination with 1,10-phenanthroline or 2,2′-bipyridine is known to render an excellent antenna and luminescence in the orange (590–620 nm) region of the electromagnetic spectrum.[41–43] A covalent attachment is formed on the surface of the iron oxide nanoparticles due to the high affinity of rhenium(I) towards pyridine ligands. *Via* this approach the iron oxide nanoparticles are kept small, so as to profit from T_1 and T_2 contributions for MRI purposes[10–12] and a rhenium antenna structure serves as a probe for optical imaging. The detailed synthetic strategy is depicted in Scheme 2 and starts with the formation of *fac*-(acetonitrile)tricarbonyl(1,10-phenanthroline)rhenium(I) triflate (ReL_1) and *fac*-(acetonitrile)tricarbonyl(2,2′-bipyridine)-rhenium(I) triflate (ReL_2) *via* a literature procedure.[42] The acid functionalized iron oxide nanoparticles (IO-COOH) were prepared *via* an optimized synthetic procedure of Bloemen *et al.*[36] and were further reacted with 4-picolylamine to produce pyridine functionalized iron oxide nanoparticles (IO-picolyl). In the final step these IO-picolyl nanoparticles were complexed with ReL_1 or ReL_2 to generate Fe_3O_4-picolyl-rhenium(I)$(CO)_3$-1,10-phenanthroline (IO-ReL_1) or Fe_3O_4-silica-picolyl-rhenium(I)$(CO)_3$-2,2′-bipyridine (IO-ReL_2), respectively.

Characterization

The nanoparticles were also characterized by X-ray powder diffraction (XRD) (ESI†) and showed strong resemblance to the crystalline pattern of magnetite cubic iron oxide nanoparticles (JPDS 19-629).

TEM images of Fe_3O_4-oleate nanoparticles have shown that they are faceted with a diameter of 8.6 ± 0.6 nm (Fig. 1a and d). After silanization and complexation with rhenium on the surface of the nanoparticles a small increase in overall size was observed, but neither change in morphology nor agglomeration was

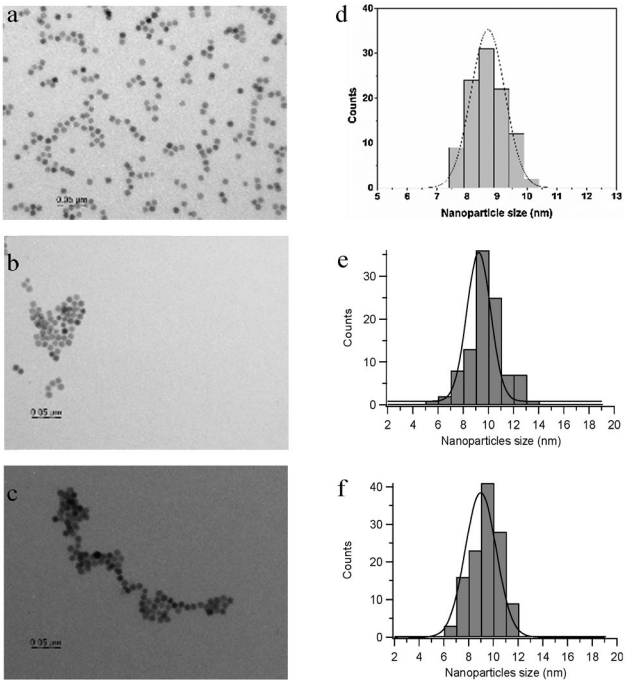

Fig. 1 TEM images of the iron oxide nanoparticles. (a) Fe_3O_4-oleate nanoparticles, (b) Fe_3O_4-ReL_2 nanoparticles, and (c) Fe_3O_4-ReL_1 nanoparticles; (d) size distribution of the Fe_3O_4-oleate nanoparticles after measuring 100 nanoparticles; (e) size distribution of the Fe_3O_4-ReL_2 nanoparticles after measuring 100 nanoparticles and (f) size distribution of the Fe_3O_4-ReL_1 nanoparticles after measuring 120 nanoparticles.

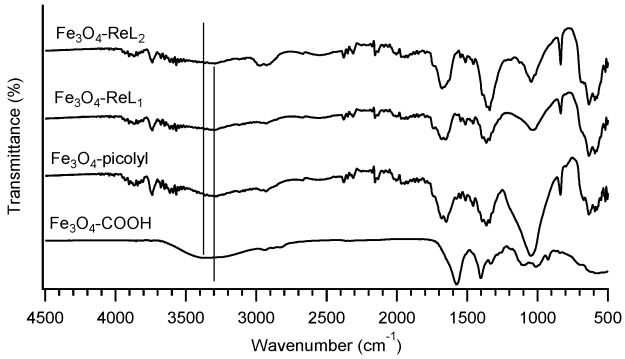

Fig. 2 FT-IR spectra of Fe_3O_4-picolyl-ReL_1 and Fe_3O_4-picolyl-ReL_2.

Table 1 Transitions observed in the FT-IR spectrum for Fe_3O_4-picolyl-ReL_1 and Fe_3O_4-picolyl-ReL_2 in comparison to Fe_3O_4-picolyl. All the transitions are displayed as wavenumbers (cm^{-1}). The symmetric and asymmetric stretches are denoted as (s) or (a)

Transition	Fe_3O_4-picolyl (cm^{-1})	Fe_3O_4-picolyl-ReL_1 (cm^{-1})	Fe_3O_4-picolyl-ReL_2 (cm^{-1})
C═O stretch	1682 (a) 1653 (s)	1686 (a) 1666 (s)	1688 (a) 1655 (s)
Aliphatic C–H stretch and C–H_2 stretch	2876 2937 2984	2880 2932 2991	2864 2937 2991
Aromatic C–H stretch	~3084	~3088	~3088
N–H stretch (amide)	3298	3311	3314

observed. As shown in Fig. 1 the size of Fe_3O_4-ReL_1 was found to be 8.9 ± 1.4 nm while the size of Fe_3O_4-ReL_2 is 9.2 ± 1.3.

Dynamic light scattering (DLS) of 0.1 wt% dispersions of IO-ReL_1 and IO-ReL_2 in water (ESI†) was carried out to investigate the hydrodynamic diameter of the particles, *i.e.* the solvated diameter of the nanoparticles, which is important for *in vivo* applications. The hydrodynamic diameter for both nanoparticles was found to be very similar in size and distribution, being 28.5 ± 0.1 nm for IO-ReL_1 and 28.52 ± 0.06 nm for IO-ReL_2.

The conversion of Fe_3O_4-COOH into Fe_3O_4-picolyl was conveniently followed by fourier transform infrared spectroscopy (Fig. 2, and Table 1) as the corresponding IR peaks have been previously well assigned in the literature.[36,44–49] A characteristic shift of the asymmetric and symmetric C═O stretches at 1581 cm^{-1} and 1555 cm^{-1} of the carboxylate group in Fe_3O_4-COOH to 1681 cm^{-1} and 1653 cm^{-1}, respectively, in Fe_3O_4-picolyl derivatives directly proves the conversion of the carboxylate group into an amide functionality. Furthermore the aliphatic CH_2 and CH asymmetric and symmetric stretches of *N*-[(3-trimethoxysilyl)-propyl] ethylenediamine triacetic acid of the Fe_3O_4-COOH located at 2835 cm^{-1}, 2889 cm^{-1} and 2945 cm^{-1} have been shifted in the spectrum of Fe_3O_4-picolyl at 2876 cm^{-1}, 2937 cm^{-1} and 2984 cm^{-1}. The new small peaks observed at higher wavenumbers (range 3050–3100 cm^{-1}) in the spectrum of Fe_3O_4-picolyl indicate aromatic C–H stretches of the pyridine ring at around 3084 cm^{-1}. The free O–H stretch visible for Fe_3O_4-COOH at 3344 cm^{-1} has decreased in intensity and migrated to 3298 cm^{-1} upon transformation into an amide bond (see Fig. 2, vertical lines). The reaction of Fe_3O_4-picolyl with ReL_1 or ReL_2 was also followed by infrared spectroscopy. However in this case the FTIR technique was not very informative as only small changes resulting from the aversion of conjugation were observed This might be due to the fact that only a fraction of picolyl groups has been effectively complexed with Re(I) resulting in low concentration of the rhenium complexes on the surface of the nanoparticles.

Total reflection X-ray fluorescence (TXRF) is a method which is frequently used to determine the elemental composition of the nanocomposites[45,50–52] and is excellent in verifying whether rhenium complexes were coupled to the surface of the magnetic nanoparticles. The ratio of rhenium *versus* iron and the overall concentration of each sample can be acquired *via* this technique with a high sensitivity. The TXRF results are given in Table 2. From these results also the concentration of rhenium complex per nanoparticle can be calculated knowing that the crystal phase of iron oxide nanoparticles is cubic (Fig. S1 and S2, ESI†) and that the unit cell has an inverse spinel structure (JPDS 19-629). Theoretical calculations performed and reported in the ESI† reveals that 201 084 ReL_1 or 210 554 ReL_2 complexes cover the surface of one Fe_3O_4 nanoparticle, which relates to 3.34 × 10^{-19} moles ReL_1 and 3.50 × 10^{-19} moles ReL_2 per nanoparticle. Since the nanoparticles were purified magnetically

Table 2 TXRF results of the iron oxide nanoparticles with ReL_1 and ReL_2 complexes on the surface

	Fe (%)	Re (%)	Fe (mM)	Re (mM)	Re/NP (mol)
Fe_3O_4-ReL_1	100	1.49	1.85	0.03	3.34×10^{-19}
Fe_3O_4-ReL_2	100	1.56	1.68	0.03	3.50×10^{-19}

(3 times) we can conclude that the rhenium complexes were effectively coupled to the nanoparticles.

Photophysical properties

The electronic absorption spectra of the complexes ReL_1, ReL_2, Fe_3O_4-ReL_1 and Fe_3O_4-ReL_2 are shown in Fig. 3. All ReL complexes show intense characteristic intraligand $\pi \rightarrow \pi^*$ transitions of phenanthroline and bipyridine in the range of 220–320 nm. An extra hump is observed in the absorbance spectrum at 360 nm and 370 nm for bipyridine and phenanthroline, respectively, though with a much smaller molar extinction coefficient than the IL $\pi \rightarrow \pi^*$ transitions. This peak can be attributed to the $d\pi(Re) \rightarrow \pi^*(L)$ ^{1}MLCT transition.[53] The difference in energy between the bipyridine and the phenanthroline MLCT band is caused by a difference in the π-accepting nature of the ligands.[43] Additional proof for the successful complexation of $ReL_{1,2}$ to Fe_3O_4 is derived from the absorbance spectrum of the Fe_3O_4-$ReL_{1,2}$ nanoparticles. Iron oxide nanoparticles are well known to show Rayleigh scattering[54] in the UV-Vis region of the electromagnetic spectrum. Thus they should exhibit an exponential decay in the absorbance spectrum, but due to $ReL_{1,2}$ attached to the surface small shoulders are disturbing this exponential decay. Especially the ^{1}MLCT band (at 370 nm) can clearly be distinguished in the absorbance spectrum.

Rhenium(I) emission has been previously examined as a potential luminophore for biomedical applications and the emission range depends greatly on the chemical environment of the metal-ion.[55] Irradiation in the spin-allowed ^{1}MLCT band at 395 nm gives a structureless ^{3}MLCT emission profile at 585 nm and 592 nm for Fe_3O_4-ReL_1 and Fe_3O_4-ReL_2, respectively (Fig. 3) as was expected from the literature.[56] The reason for this small blue shift between the phenanthroline derivative and the bipyridine derivative might be due to rigidochromism,[53] the difference in emission maximum due to differences in the rigidity of the environment.

Relaxometry

The efficiency of the nanoparticles as MRI contrast agents is related to their ability to enhance the water proton longitudinal and transverse relaxation rates. This is usually reported as the relaxivity and defined as the increase in relaxation rate induced by one millimole of iron per liter. The relaxation induced by superparamagnetic nanoparticles is described by the outer sphere mechanism which depends on the following parameters: the diffusion of water (D), the Néel relaxation time (τ_N) related to the relaxation of the global magnetic moment of the particle, the magnetization of the particle (and thus the saturation magnetization M_{sat}) and the radius of the magnetic particle (r). It is to be reminded that the mean magnetic moment of the particle increases with the applied magnetic field to reach its saturation value whereas the Néel relaxation time increases exponentially with the volume of the particle. The modulation of the interaction results either from τ_N or τ_D (with $\tau_D = r^2/D$). At high magnetic fields, the Néel relaxation is not possible since the magnetic moment is locked onto the magnetic field and the modulation is due to τ_D. At low magnetic fields, both τ_N and τ_D can modulate the interaction. For very

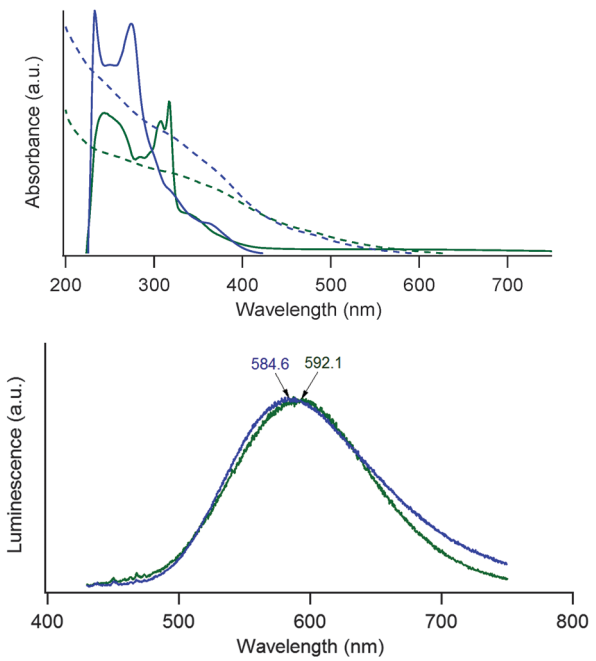

Fig. 3 Top: absorbance spectra of ReL_1 (phenanthroline – blue dashed line), ReL_2 (bipyridine – green dashed line), Fe_3O_4-ReL_1 (phenanthroline – blue solid line) and Fe_3O_4-ReL_2 (bipyridine – green solid line). Bottom: normalized luminescence spectra of Fe_3O_4-ReL_1 (phenanthroline – blue) and Fe_3O_4-ReL_2 (bipyridine – green) upon excitation at 395 nm. The maximum emission wavelength of both Fe_3O_4-ReL_1 and Fe_3O_4-ReL_2 is denoted above the spectrum in blue and green, respectively.

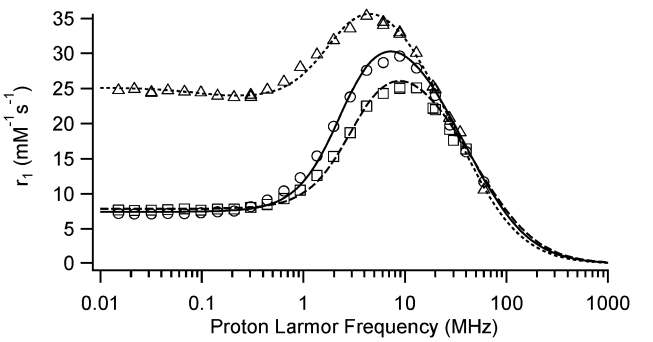

Fig. 4 Experimental (physiological conditions) and fitted longitudinal relaxivity (r_1) of the Fe_3O_4-ReL_1 (phenanthroline) and Fe_3O_4-ReL_2 (bipyridine) nanoparticles and Sinerem®. The experimental values for Fe_3O_4-ReL_1 are visualized by squares whilst for Fe_3O_4-ReL_2 they are visualized by circles and for Sinerem® they are visualized by triangles. The fitted profiles are given by a dashed line, a solid line and a dotted line, respectively.

Table 3 Relaxometric values of Fe_3O_4-ReL_1 (phenanthroline) and Fe_3O_4-ReL_2 (bipyridine) both measured at 60 MHz under physiological conditions and compared to Sinerem®

	r_1 (mM^{-1} s^{-1})	r_2 (mM^{-1} s^{-1})	r_2/r_1
Fe_3O_4-Re-L_1	11.5	92.95	8.09
Fe_3O_4-Re-L_2	11.7	97.47	8.33
Sinerem®	10.6	61.7	5.84

Table 4 Saturation magnetization, radius and Néel relaxation time obtained from the theoretical fitting of the proton NMRD profiles. The diffusion coefficient was fixed to 3×10^{-9} m^2 s^{-1}

Parameter	Fe_3O_4-ReL_1	Fe_3O_4-ReL_2	Sinerem®
M_{SAT} (A m^2 kg^{-1})	46.0 ± 0.2	45.0 ± 0.2	42.4 ± 0.3
Diameter (nm)	10.40 ± 0.06	11.44 ± 0.06	12.28 ± 0.1
τ_N (ns)	0.82 ± 0.01	0.76 ± 0.01	6.25 ± 0.13

small USPIO particles, a low field dispersion can be observed since the magnetization is less locked to the anisotropy directions as shown in the NMRD profile of Sinerem® (Fig. 4).

The evolution of the longitudinal relaxivity, visualized in Fig. 4, of Fe_3O_4-ReL_1 and Fe_3O_4-ReL_2 as a function of the applied magnetic field is typical of superparamagnetic iron oxide nanoparticles (Table 3). At high magnetic fields, r_1 values are similar for Fe_3O_4-ReL_1, Fe_3O_4-ReL_2 and Sinerem® but at low magnetic fields, Sinerem® has a higher longitudinal relaxivity.

The saturation magnetization expressed in A m^2 per kg of ferrite obtained from the theoretical fitting (Table 4) of these curves[38–40] is similar for both types of particles, typical for iron oxide nanoparticles with a silane coating and close to the value found for Sinerem®. The diameters found from the fitting are comparable to those obtained by TEM although somewhat larger. This effect results from the fitting procedure of the NMRD profiles, which depends on the distance of the closest approach of water molecules to the superparamagnetic center whereas TEM data give the diameter of the magnetic core. The unusually low value of τ_N found for Fe_3O_4-ReL_1 and Fe_3O_4-ReL_2 seems to indicate that the magnetization is poorly locked to the anisotropy directions. The large values of r_2 obtained for these nanoparticles show their potential as T_2 relaxation agents especially compared to Sinerem®.

Conclusions

In this paper successful synthesis of the assembly consisting of the iron oxide nanoparticles and the rhenium complexes was reported. The overall size of the particles increased minimally upon silanization and coordination of the rhenium complexes, as proven by TEM and NMRD measurements. Sensitized luminescence of the rhenium was found in the orange region of the electromagnetic spectrum at 585 nm (IO-ReL_1) and 592 nm (IO-ReL_2) upon irradiation at 395 nm, which could be used for optical imaging. The relaxometric study performed at a magnetic field strength of 60 MHz showed high r_2-values of the nanoparticles of nearly 100 mM^{-1} s^{-1}, making them superior to previously commercial Sinerem®. Therefore, the proposed materials have potential use as probes for bimodal MRI and optical imaging. More efforts will be devoted to testing the compatibility using SPECT, the stability in cells and possible radiotherapy applications in order to explore the promising multimodal/theranostic character of these novel nano-assemblies.

Acknowledgements

This work was financially supported by grant G.0618.11N of the Fund for scientific research Flanders (FWO-V) and the Agency for Innovation by Science and Technology in Flanders (IWT). SC and MB are grateful for support from the IWT. LVE and SL thank the Walloon Region (program First spin-off), the FNRS (Fond National de la Recherche Scientifique), the UIAP VII and ARC Programs (AUWB-2010-10/15-UMONS-5) of the French Community of Belgium and the Center for Microscopy and Molecular Imaging (CMMI, supported by the European Regional Development Fund and the Walloon Region). SC and TNPV would like to thank Jeroen Jacobs, Prof. Koen Binnenmans and Prof. Luc Vanmeervelt for the use and help with the powder X-ray diffractions of the samples. Also we would like to thank Prof. Johan Billen from the department of Biology at KU Leuven for the TEM measurements and Prof. Christine Kirschhock from the department of Microbial and Molecular Systems at KU Leuven for the DLS measurements.

Notes and references

1 F. Stuker, J. Ripoll and M. Rudin, *Pharmaceutics*, 2011, **3**, 229–274.
2 E. J. Sutton, T. D. Henning, S. Boddington, S. Demos, C. Krug, R. Meier, J. Kornak, Z. Shoujun, R. Baehner, S. Sharifi and H. Daldrup-Link, *Mol. Imaging*, 2010, **9**, 278–290.
3 W. Stummer, U. Pichlmeier, T. Meinel, O. D. Wiestler, F. Zanella and H.-J. J. Reulen, *Lancet Oncol.*, 2006, **7**, 392–401.
4 J.-M. Shen, F.-Y. Gao, T. Yin, H.-X. Zhang, M. Ma, Y.-J. Yang and F. Yue, *Pharmacol. Res.*, 2013, **70**, 102–115.
5 J. Grimm, D. G. Kirsch, S. D. Windsor, C. F. B. Kim, P. M. Santiago, V. Ntziachristos, T. Jacks and R. Weissleder, *Proc. Natl. Acad. Sci. U. S. A.*, 2005, **102**, 14404–14409.
6 T. Heidt and M. Nahrendorf, *NMR Biomed.*, 2013, **26**, 756–765.
7 S. Laurent, D. Forge, M. Port, A. Roch, C. Robic, L. Vander Elst and R. N. Muller, *Chem. Rev.*, 2008, **108**, 2064–2110.
8 Y.-X. J. Wang, *Quant. Imaging Med. Surg.*, 2011, **1**, 35–40.
9 R. Qiao, C. Yang and M. Gao, *J. Mater. Chem.*, 2009, **19**, 6274–6293.
10 W.-Y. Huang and J. J. Davis, *Dalton Trans.*, 2011, **40**, 6087–6103.
11 K. E. Kellar, D. K. Fujii, W. H. Gunther, K. Briley-Saebø, A. Bjørnerud, M. Spiller and S. H. Koenig, *J. Magn. Reson. Imaging*, 2000, **11**, 488–494.

12 D. Jańczewski, Y. Zhang, G. K. Das, D. K. Yi, P. Padmanabhan, K. K. Bhakoo, T. T. Y. Tan and S. T. Selvan, *Microsc. Res. Tech.*, 2011, **74**, 563–576.
13 M. Di Marco, C. Sadun, M. Port, I. Guilbert, P. Couvreur and C. Dubernet, *Int. J. Nanomed.*, 2007, **2**, 609–622.
14 Y. T. Lim, M. Y. Cho, J. K. Kim, S. Hwangbo and B. H. Chung, *ChemBioChem*, 2007, **8**, 2204–2209.
15 Y. Xu, S. Palchoudhury, Y. Qin, T. MacHer and Y. Bao, *Langmuir*, 2012, **28**, 8767–8772.
16 Y. Xu, J. Sherwood, Y. Qin, D. Crowley, M. Bonizzoni and Y. Bao, *Nanoscale*, 2014, **6**, 1515–1524.
17 C. V. Durgadas, C. P. Sharma and K. Sreenivasan, *Nanoscale*, 2011, **3**, 4780–4787.
18 W. J. M. Mulder, G. J. Strijkers, G. A. F. Van Tilborg, D. P. Cormode, Z. A. Fayad and K. Nicolay, *Acc. Chem. Res.*, 2009, **42**, 904–914.
19 L. Li, H. Li, D. Chen, H. Liu, F. Tang, Y. Zhang, J. Ren and Y. Li, *J. Nanosci. Nanotechnol.*, 2009, **9**, 2540–2545.
20 S. A. Corr, Y. P. Rakovich and Y. K. Gun'Ko, *Nanoscale Res. Lett.*, 2008, **3**, 87–104.
21 J.-M. Lei, X.-L. Xu, L. Liu, N.-Q. Yin and L.-X. Zhu, *Chin. Phys. Lett.*, 2012, **29**, 097803.
22 H. Kobayashi and M. W. Brechbiel, *Curr. Pharm. Biotechnol.*, 2004, **5**, 539–549.
23 A. J. Aaron, A. Bumb and M. W. Brechbiel, *Chem. Rev.*, 2010, **110**, 2921–2959.
24 N. Chekina, D. Horák, P. Jendelová, M. Trchová, M. J. Beneš, M. Hrubý, V. Herynek, K. Turnovcová and E. Syková, *J. Mater. Chem.*, 2011, **21**, 7630–7639.
25 L. Frullano and T. J. Meade, *JBIC, J. Biol. Inorg. Chem.*, 2007, **12**, 939–949.
26 A. Louie, *Chem. Rev.*, 2010, **110**, 3146–3195.
27 M.-K. Yoo, I.-K. Park, H.-T. Lim, S.-J. Lee, H.-L. Jiang, Y.-K. Kim, Y.-J. Choi, M.-H. Cho and C.-S. Cho, *Acta Biomater.*, 2012, **8**, 3005–3013.
28 P. Howes, M. Green, A. Bowers, D. Parker, G. Varma, M. Kallumadil, M. Hughes, A. Warley, A. Brain and R. Botnar, *J. Am. Chem. Soc.*, 2010, **132**, 9833–9842.
29 E. D. Smolensky, Y. Zhou and V. C. Pierre, *Eur. J. Inorg. Chem.*, 2012, 2141–2147.
30 V. Sreeja, K. N. Jayaprabha and P. A. Joy, *Appl. Nanosci.*, 2014, 1–6.
31 A. Ruiz-Medina, E. J. Llorent-Martínez, P. Ortega-Barrales and M. L. F. Córdova, *Appl. Spectrosc. Rev.*, 2011, **46**, 561–580.
32 T. Haley and F. D. Cartwright, *J. Pharm. Sci.*, 1968, **57**, 321–323.
33 T. Santonen and A. Aitio, Manganese and Rhenium, *Patty's Toxicology*, vol. 39, 2012.
34 D. Maggioni, P. Arosio, F. Orsini, A. M. Ferretti, T. Orlando, A. Manfredi, E. Ranucci, P. Ferruti, G. D'Alfonso and A. Lascialfari, *Dalton Trans.*, 2014, **43**, 1172–1183.
35 I. J. Bruce and T. Sen, *Langmuir*, 2005, **21**, 7029–7035.
36 M. Bloemen, W. Brullot, T. T. Luong, N. Geukens, A. Gils and T. Verbiest, *J. Nanopart. Res.*, 2012, **14**, 1100–1109.
37 *CrysAlisPro*, Agilent Technologies, 2013.
38 A. Roch, P. Gillis, A. Ouakssim and R. Muller, *J. Magn. Magn. Mater.*, 1999, **201**, 77–79.
39 A. Roch, Y. Gossuin, R. N. Muller and P. Gillis, *J. Magn. Magn. Mater.*, 2005, **293**, 532–539.
40 P. Gillis, F. Moiny and R. A. Brooks, *Magn. Reson. Med.*, 2002, **47**, 257–263.
41 M. Wrighton and D. L. Morse, *J. Am. Chem. Soc.*, 1974, **96**, 998–1003.
42 T. Koullourou, L. S. Natrajan, H. Bhavsar, S. J. A. Pope, J. Feng, J. Narvainen, R. Shaw, E. Scales, R. Kauppinen, A. M. Kenwright and S. Faulkner, *J. Am. Chem. Soc.*, 2008, **130**, 2178–2179.
43 C. C. Ko, C. O. Ng and S. M. Yiu, *Organometallics*, 2012, **31**, 7074–7084.
44 I. F. Dudley Williams, *Spectroscopic Methods in Organic Chemistry*, McGraw-Hill education, Berkshire, 6th edn, 2008.
45 M. Bloemen, S. Vandendriessche, V. Goovaerts, W. Brullot, M. Vanbel, S. Carron, N. Geukens, T. Parac-Vogt and T. Verbiest, *Materials*, 2014, **7**, 1155–1164.
46 M. Bloemen, D. Debruyne, P.-J. Demeyer, K. Clays, A. Gils, N. Geukens, C. Bartic and T. Verbiest, *RSC Adv.*, 2014, **4**, 10208–10211.
47 M. Bloemen, B. Sutens, W. Brullot, A. Gils, N. Geukens and T. Verbiest, *ChemPlusChem*, 2014, **80**, 50–53.
48 M. Bloemen, T. Van Stappen, P. Willot, J. Lammertyn, G. Koeckelberghs, N. Geukens, A. Gils and T. Verbiest, *PLoS One*, 2014, **9**, e109475.
49 F. Monnaie, W. Brullot, T. Verbiest, J. De Winter, P. Gerbaux, A. Smeets and G. Koeckelberghs, *Macromolecules*, 2013, **46**, 8500–8508.
50 D. Dupont, J. Luyten, M. Bloemen, T. Verbiest and K. Binnemans, *Ind. Eng. Chem. Res.*, 2014, **53**, 15222–15229.
51 D. Dupont, W. Brullot, M. Bloemen, T. Verbiest and K. Binnemans, *ACS Appl. Mater. Interfaces*, 2014, **6**, 4980–4988.
52 L. Borgese, A. Zacco, E. Bontempi, P. Colombi, R. Bertuzzi, E. Ferretti, S. Tenini and L. E. Depero, *Meas. Sci. Technol.*, 2009, **20**, 084027.
53 A. J. Lees and C. Long, *Topics in Organometallic Chemistry*, Springer Science & Business Media, 2010, vol. 29, pp. 37–71.
54 C. F. Bohren and D. R. Huffman, *Absorption and Scattering of Light by Small Particles*, 1998.
55 K. K. W. Lo, *Top. Organomet. Chem.*, 2010, **29**, 115–158.
56 E. Wolcan, G. Torchia, J. Tocho, O. E. Piro, P. Juliarena, G. Ruiz and M. R. Féliz, *J. Chem. Soc., Dalton Trans.*, 2002, 2194–2202.

